

Differentiable design of the PIAA-ZWFS: a flexible wavefront sensor that approaches the fundamental limit

A. K. Taras^{1,*}, S. Y. Haffert¹, and L. Desdoigts¹

¹Leiden Observatory, Leiden University, PO Box 9513, 2300 RA Leiden, The Netherlands

ABSTRACT

Context. Extreme adaptive optics (AO) is necessary for high contrast astronomy at scales of the habitable zone of nearby systems.

Aims. We seek to evaluate wavefront sensors that approach fundamental limits of wavefront sensing, enabling adaptive optics systems to run faster or on fainter targets.

Methods. We present the phase-induced amplitude apodisation Zernike wavefront sensor (PIAA-ZWFS): an adaptation of the conventional Zernike wavefront sensor (ZWFS) that leverages lossless apodisation of the pupil to concentrate the starlight in the focal plane. We optimise and evaluate the sensor with a differentiable modelling framework, drawing on concepts from Bayesian experimental design to minimise the variance of a maximum likelihood estimator that uses the system in the high Strehl regime.

Results. Our architecture shows state-of-the-art performance in simulation for different apertures, bandwidths, photon fluxes and source sizes, closing the gap to the fundamental limit by a factor 10 (2.5) compared to the conventional ZWFS (optimised ZWFS) in a typical photon-limited case. For extended sources, we show that even an ideal point source WFS rapidly becomes sub-optimal, and our system outperforms it for stellar diameters larger than $0.8\lambda/D$. We verify that these gains do not come at the cost of dynamic range with either linear or non-linear reconstructors. Finally, we present a proof that there must be a trade-off between the information gained about amplitude and phase errors for any wavefront sensor.

Conclusions. The PIAA-ZWFS is a viable wavefront sensor operating near the fundamental sensitivity limits.

Key words. adaptive optics – high angular resolution

1. Introduction

Extreme adaptive optics (AO) systems are necessary for the detection and characterisation of exoplanets from ground based telescopes (Guyon 2018). In particular, instruments on the coming generation of Extremely Large Telescopes (ELTs) could extend the list of directly imaged exoplanets to include habitable zone planets around nearby low mass stars (Kasper et al. 2021; Males et al. 2024). Assuming such a system can maintain diffraction limited and background noise dominated performance, the exoplanet scientific yield of instruments with a telescope diameter of D scales almost as D^4 (Males et al. 2021), as opposed to other applications (e.g. radial velocity surveys) which scale as D^2 .

In order to achieve diffraction limited performance, wavefront sensors (WFSs) must be very sensitive to phase aberrations, enabling the control loop to function well at kilohertz rates. Different WFSs are known to have different sensitivities (Ragazzoni & Farinato 1999; Guyon 2005). The sensitivity limit given a number of photons has been known for some time (Paterson 2008) but no architectures have been demonstrated in hardware that approach this limit. For the past two decades the phase contrast technique used in the Zernike wavefront sensor (ZWFS) (Zernike 1934; N'Diaye et al. 2013) has been regarded as most sensitive in the presence of photon noise. This architecture focuses starlight onto a mask that shifts the phase of the core, resulting in interference that reveals the phase aberrations when the pupil plane is imaged. Previous work has shown that it is possible to optimise the phase mask structure to max-

imise the sensitivity in the linear (Chambouleyron et al. 2022) or, through joint optimisation with a neural network, non-linear (Landman et al. 2022) regime.

Beyond ground based instruments, more sensitivity wavefront sensors are becoming important for the next generation of high contrast, space based missions, where picometer wavefront sensing is required (Steeves et al. 2020). For such applications the time needed to flatten the wavefront can be reduced by hours by employing higher sensitivity wavefront sensors.

In this work, we explore the phase-induced amplitude apodisation Zernike wavefront sensor (PIAA-ZWFS) for use in a second stage adaptive optics system. This sensor was briefly introduced previously in Haffert et al. (2023). It consists of two relatively simple modifications to the classical ZWFS: the addition of phase-induced amplitude apodization (PIAA) lenses to concentrate starlight on the phase mask and the freedom to construct a multi-level phase mask at the focal plane.

Our approach optimises this new architecture to minimise the variance of an unbiased, maximum likelihood estimator when estimating the phase at the pupil plane. This is similar to, but not the same as, previous work (Chambouleyron et al. 2022; Landman et al. 2022) that optimised the information gained from phase aberrations at different spatial frequencies one at a time. Our method correctly captures possible crosstalk in the system and better reflects the expected residuals in closed loop operation (explicitly, the loss is the residual phase root mean square (RMS) of the system). First, we develop the Fisher information framework of wavefront sensing, deriving previous results on sensitivity limits from this different perspective. Next, we evaluate the performance of the PIAA-ZWFS in a variety of scenarios: different apertures, stellar magnitude, bandwidth

* Corresponding author: taras@strw.leidenuniv.nl

and stellar size. These results are compared to variants of the ZWFS and an ideal wavefront sensor that saturates the information limit. We also show that each component of the PIAA-ZWFS is important in our ablation study, and that the system can still reconstruct the wavefront with the same dynamic range as existing sensors.

2. The PIAA-ZWFS

2.1. System Overview

Figure 1 depicts a pencil sketch of the PIAA-ZWFS architecture and our optimisation approach. The optics are relatively minimal by design, with a pair of aspheric PIAA lenses after the pupil and before the detector. There is also a phase mask at the focus.

The architecture contains two significant differences from a conventional ZWFS: the pair of PIAA lenses and more degrees of freedom in the phase mask. These modifications are well motivated by considering the ZWFS as an interferometer, where the phase shifted beam interferes with the beam outside the phase mask. An interferometer has maximal response when amplitudes are equal and opposite phase, which requires the ‘mode’ of the beam through the phase mask to match the beam outside the mask. For cases where the pupil is a top hat function, the optimal phase mask resembles the Airy pattern (Chambouleyron et al. 2022; Landman et al. 2022). Optimising the phase mask without apodisation, however, requires a mask that has large extent, and hence performs worse at larger bandwidth. Slepian (1965) first studied the problem of apodisation to suppress side lobes of the diffraction pattern. It is known that the Fourier transform of a function with discontinuous m^{th} derivative is asymptotically a power law with exponent $-(m + 1)$ (Bracewell & Kahn 1966), and hence apodisation in the pupil plane restricts the size of the phase mask necessary for mode matching significantly. Noting that the information gained from a wavefront sensor is measured per photon, we limit ourselves to phase-induced apodisation (Guyon 2003) only, which is lossless up to reflection losses.

To fine tune the overall architecture, our optimisation approach leverages differentiable simulation. We apply a set of orthonormal optical path difference (OPD) probes at the pupil and compute the derivative of the wavefront sensor image $\partial I / \partial a_k$. These responses are used to compute the information gained about the aberrations in the pupil plane. We optimise the system rapidly using gradient based methods, computing the derivative of this loss function with respect to lens asphere coefficients $\alpha_{\text{qbf}s}$ and phase mask thicknesses at different radii α_{mask} .

The PIAA ZWFS has a relatively straightforward path towards manufacturing. PIAA lenses have already been manufactured successfully, while advances in grayscale lithography (Grushina 2019), liquid crystals (Doelman et al. 2017) or optical metasurfaces (Chang et al. 2018) allow for the creation of masks with this control of phase.

2.2. Theory

We begin by outlining our formulation of the wavefront sensing problem, defining the Fisher information and drawing theoretical insights about the space of possible designs.

Let the input field of a coherent point source entering the system be defined as

$$E_i = A(x, y) \exp(i\phi(x, y)) / S_A, \quad (1)$$

where (x, y) are the coordinates in the detector plane, A is the aperture function (1 everywhere inside the aperture and 0 out-

side), S_A is the aperture area as a normalising term (such that the total power of E_i is unity) and ϕ is the phase.

Drawing on previous work about the kernel formalism for wavefront sensors (Fauvarque et al. 2019), the output electric field from an optical system is defined via a linear operator C as

$$E_o(x', y') = \iint K(x', y', x, y) E_i(x, y) dx dy =: C\{E_i\}, \quad (2)$$

where $K(x', y', x, y)$ describes the optical system and $E_o(x', y')$ is the output electric field, defined on detector coordinates (x', y') . Coordinates are dropped onwards for brevity. This operator is linear in E_i due to the linearity of the integral. The intensity measured is just $I = N_{\text{ph}} |E_o|^2$.

Let $\{W_k(x, y)\}, k \in \mathbb{N}_0$ be an orthonormal basis set with respect to the usual norm over the pupil, i.e.

$$\langle W_i, W_j \rangle = \iint A W_i W_j dx dy = \begin{cases} 1 & i = j \\ 0 & i \neq j \end{cases}. \quad (3)$$

Without loss of generality, let W_0 be the piston term that we do not attempt to sense.

The aberrations in the pupil plane are then expanded as

$$\phi = \sum_{k>0} a_k W_k, \quad (4)$$

where the piston term is omitted as optical systems are invariant to global phase.

The wavefront sensing problem is: given measurements of I , estimate the phase aberrations at the pupil plane a_k . The Fisher information framework enables us to quantify how well constrained the coefficients a_k are given a system C and an input field E_i (assumed to be a flat wavefront for closed loop operation).

The Fisher information of such a system under a combination of photon and read noise is

$$\text{FI}_{a_k a_l} = \sum_j \frac{(\partial_{a_k} I)(\partial_{a_l} I)}{I + \sigma_R^2} \quad (5)$$

where the sum is taken over all pixels in the detector and σ_R is the read noise of the detector. We include a proof of this and relations to previous work in Appendix A. While previous work (Chambouleyron et al. 2023) derived sensitivity in the photon or read noise cases, the above allows us to treat situations between the two, and correctly deal with cases where some pixels have more flux than others.

Equation 5 requires the derivative of the intensity with respect to the coefficient of the phase aberration. This can be computed efficiently by applying the chain rule

$$\begin{aligned} \frac{\partial_{a_k} I}{N_{\text{ph}}} &= 2\Re \{E_o^* \partial_{a_k} E_o\} \\ &= 2\Re \{E_o^* C\{\partial_{a_k} E_i\}\} \\ &= 2\Re \{E_o^* C\{iW_k E_i\}\}, \end{aligned} \quad (6)$$

noting that we may interchange the derivative and C operators as the integration bounds do not depend on coefficients and E_i is differentiable in the aberration coefficients a_k . This result illustrates that the Jacobian of the intensity depends on the output electric field and the field generated by propagating $W_k E_i$ through the system. Hence, the computational cost of measuring the Fisher information of an optical model with respect to

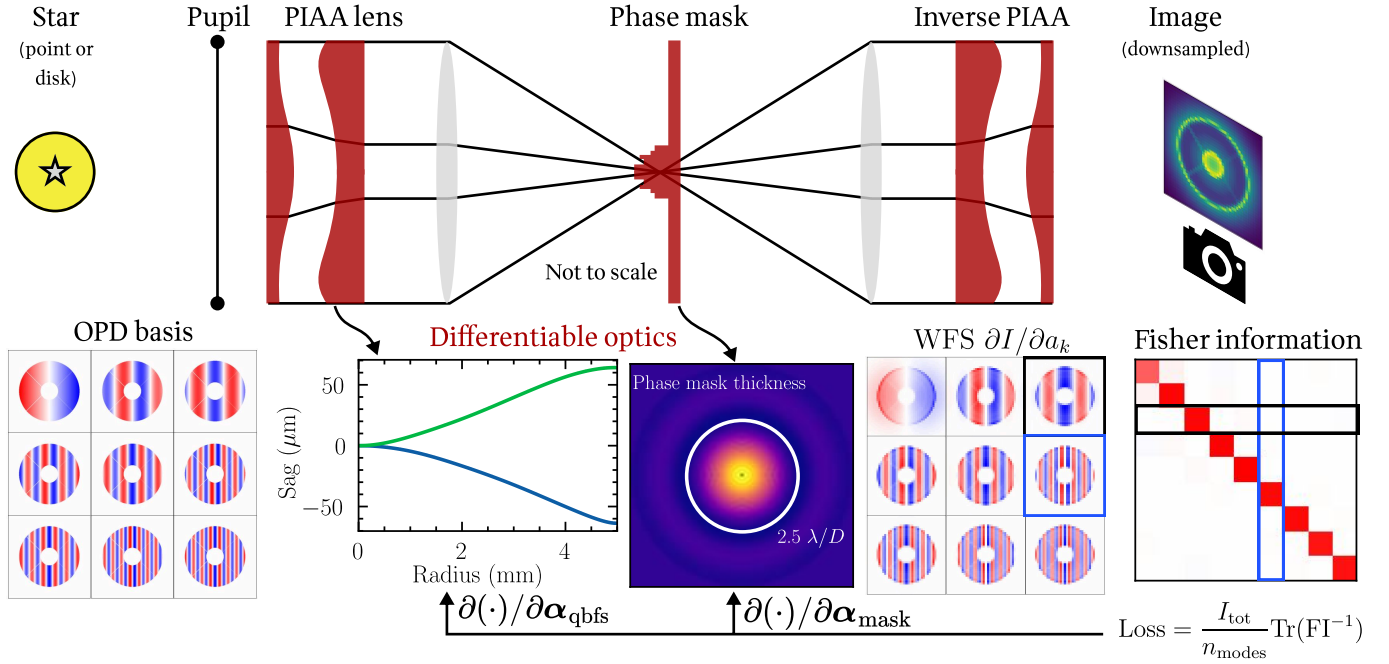


Fig. 1: Architecture of the PIAA-ZWFS and our optimisation framework. We simulate starlight from a point or resolved source through a telescope pupil. This then passes through a set of PIAA lenses for lossless apodisation, is focused on a phase mask and then re-imaged in the pupil plane through an inverse PIAA lens. The final image is formed by downsampling the intensity distribution. As the simulation is differentiable, we are able to compute the derivative of the output intensity with respect to the phase coefficient (“WFS $\partial I / \partial a_k$ ”). All pairs of the basis set are then used to calculate the Fisher information matrix of the system. The optimiser measures the average variance of a maximum likelihood estimator (given by the trace of the inverse of the Fisher information matrix) and is able to access derivatives of this metric with respect to optical prescriptions in the PIAA lenses (α_{qbfs}) and phase mask (α_{mask}), converging on an optical design that best constrains the phase estimates.

N phase aberrations is $N + 1$ optical propagations – an important factor in the tractability of the optimisation framework presented.

The information limit to the wavefront sensing problem is the bound of Equation 5 under photon noise, which has been shown to be 4 per photon per radian (Paterson 2008). These bounds are also verified in our formalism for completeness in Appendix A

We also note that Appendix A.3 presents a novel proof that the sum of the (classical or quantum) information from amplitude and phase is bounded to 4 for all non-piston modes. Thus sensors which maximise phase information necessarily lose information about amplitude variations.

It has also been previously shown that the ideal point source wavefront sensor is one that shifts the piston mode of the system by $\pi/2$ in phase and leaves all other modes unaffected (Chambouleyron et al. 2024). We can quickly confirm this in the above framework. As the zero point of the wavefront sensor is the piston mode, the output electric field is just $E_o = iA$. As the system leaves other modes unaffected, $C\{W_n E_i\} = W_n E_i = W_n$. Hence we can consider the numerator of the Fisher information (on the diagonal) in either photon or read noise cases as

$$\begin{aligned} 4N_{\text{ph}}^2 (\Im(E_o^* C\{W_n E_i\}))^2 &= 4N_{\text{ph}}^2 (\Im(iAW_n))^2 \\ &= 4N_{\text{ph}}^2 (W_n)^2. \end{aligned} \quad (7)$$

This expression integrates to unity per photon (as it is part of an orthonormal basis). One can similarly show that off-diagonal elements are zero. For cases where the zero point is not a flat wavefront, the wavefront sensor can be modified with a phase

transformation that first makes the desired zero point become a flat wavefront, and then the piston mode is shifted in phase as above.

Hence an ideal wavefront sensor saturates both the photon and read noise bounds. While the sensitivity to either doesn’t need to be the same in general for an arbitrary wavefront sensor, it is in the case of the ideal wavefront sensor.

We use a (lossless and achromatic) simulation of such a device to illustrate the limits of all wavefront sensors in the numerical results in the following sections. This ensures any loss of sensitivity due to downsampling occurs equally in the ideal case as all others. Also, we use broadband simulations and hence define the phase aberration basis in OPD, as this better reflects the nature of the atmosphere.

Note that we have introduced this concept as the ideal *point source* wavefront sensor because, as we show, this wavefront sensor is far from ideal when it comes to extended sources.

For any sub-optimal wavefront sensor, however, it is not guaranteed that the Fisher information for cross terms ($\text{FI}_{a_k a_l}, l \neq k$) is zero. Furthermore, performance of the system is not best reflected by this information quantity directly. Rather, the performance of an adaptive optics system is typically quantified with the Strehl ratio, which in the well corrected limit depends on the RMS of the wavefront errors. Thus, the variance of each mode in a closed loop system better reflects the expected performance.

For these two reasons we do not optimise the Fisher information itself, instead the loss function used is the average variance of all modes when estimated via a maximum likelihood estimate via the trace of the covariance matrix – the inverse of the matrix

with elements $FI_{a_k a_l}$. This metric is minimised and is a standard metric in Bayesian experimental design.

2.3. Implementation in simulation

The numerical simulation is written in Python¹, leveraging the auto-differentiation provided by `jax`. The `dLux` package is used for modelling of optical components and propagation, while `hcupy` is used for apertures and PIAA initialisation.

The aberration basis set used is a Fourier basis of both sines and cosines in the x axis only (exploiting the near circular symmetry), with 7 frequencies equally spaced from 0.01 to 8 cycles per pupil. The 0.01 cycles/pupil cosine mode is removed as it resembles piston and then the modes are orthonormalised over the support of the aperture. The normalisation is such that each mode is $1\ \mu\text{m}$ in OPD. We find the converged designs do not change significantly when altering the frequencies and/or the number of basis aberrations.

The PIAA lens profiles are first initialised using a heuristic from the mode matching argument described above, but then allowed to vary during the optimisation of the sensor. The initial profile of the PIAA lenses are found by solving for the apodisation profile that is an Eigenmode of a spatial filter with diameter $2\lambda_c/D$, where λ_c is the central wavelength. The profile is then fit as a Gaussian and converted to aspherical lens parameters following the procedure outlined in Hoffnagle & Jefferson (2000). We employ the Q_{bfs} basis from Forbes (2007). This basis was originally invented as an improvement over an even polynomial expansion which was poorly suited for design and tolerancing as typical shapes required alternating signs and large coefficients, leading to numerical instabilities. The advantages of the Q_{bfs} basis for tolerancing also mean that it is a good basis for optimisation.

The phase mask thickness is defined on a basis consisting of concentric annular rings. We use 64 equally spaced annuli over 5 Airy rings, with a pixel sampling of 32 pixels per λ/D in the focal plane. For the propagation routine we leverage the semi-analytic methods presented in Soummer et al. (2007).

We note that existing approaches like different dot size ZWFSs are contained within the parametrisation above – a flat surface on each PIAA lens and a phase mask that is simply a top hat function. Our results show that the degrees of freedom given are indeed able to significantly improve the performance of the system.

Simulations are typically run with 3 wavelengths over the width of the Z band, with the exception of the bandwidth variation experiment which uses 5 wavelengths. This sampling is more than sufficient to capture wavelength dependent behaviour in the image plane with diameter $\sim 2\lambda/D$. For wavelength dependence, both the PIAA and phase mask are simulated to be made from fused silica. Further optimisation of the dispersive elements is left for future work.

2.4. Optimisation

The complete PIAA ZWFS model has 82 parameters: 64 phase mask thickness values, 8 asphere coefficients per PIAA lens and one spherical term per PIAA lens.

The optimisation uses the Broyden–Fletcher–Goldfarb–Shanno (BFGS) (Fletcher 2013) algorithm via the `optimistix` package (Rader et al. 2024). This method directly uses the gradients available and also

estimates the hessian of the optimisation function, resulting in faster convergence and robustness to different parameter scales (which are expected in problems of this nature). To keep results comparable between different experiments and provide robust optimisation, the loss function is normalised per photon and per mode. Furthermore, the model parameters are implemented in μm , such that all are close to unity.

All optimisations except the resolved sources were executed locally on a laptop grade graphics processing unit (GPU) (6 GB NVIDIA RTX PRO 500 Blackwell), with each optimisation no more than a few minutes. The resolved source optimisations were run on a NVIDIA L4 GPU and took less than half an hour for each optimisation.

3. Results

As a reminder, the loss function (average variance of estimates from a maximum likelihood estimator) used in this work has units of $(\mu\text{m OPD})^2$ per photon per frame. For example, a loss value of 9×10^{-3} indicates that the variance of the error the fit on a frame with 10^9 photons will be $9 \times 10^6 \mu\text{m}^2$ OPD per mode, or a standard deviation of 3 nm per mode.

3.1. The PIAA-ZWFS can saturate the information bound at high spatial frequencies

Here we present a verification of the results shown previously by Haffert et al. (2023), where the PIAA-ZWFS is able to saturate the wavefront sensing information limit for high frequency aberrations. We also illustrate how our approach of minimising the covariance finds a different solution. This experiment is conducted using the whole Z band on the Magellan aperture with a high pupil sampling. The results are illustrated in Figure 2. When

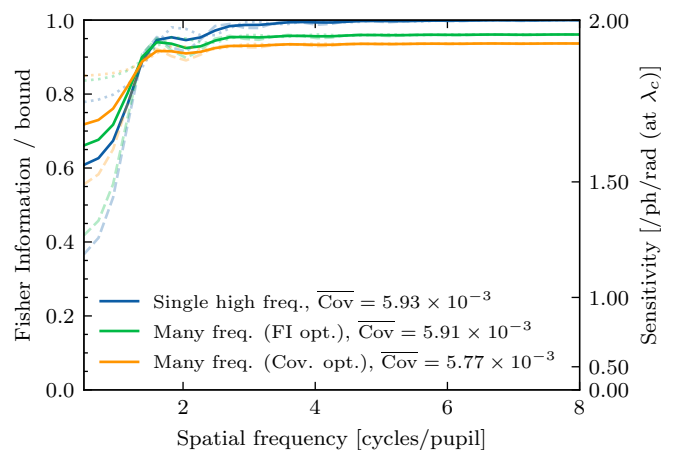


Fig. 2: Verification that PIAA-ZWFS can reach the sensitivity limit for high spatial frequencies. The information gained, normalised to that of an ideal wavefront sensor as a function of the spatial frequency of the applied mode. Solid lines show the quadrature averaged information gain to a single sine (dashed) or cosine (dotted) Fourier mode. Sensors are either optimised for a single high frequency (blue), to maximise the Fisher information of multiple frequencies (green) or to minimise the covariance to multiple frequencies (orange). Legend text shows the average variance of an estimator of each mode over the full basis set. For comparison with other work, the right axis marks the sensitivity ($= \sqrt{FI}$ per radian at the centre wavelength).

¹ All code can be found here [🔗](#)

optimising for a single high frequency (5 cycles/pupil, blue) the sensor reaches the fundamental limit at high frequencies, at the cost of lower information gain at low frequencies. In this case, minimising the average variance has the same solution as maximising the information gained (up to optimisation termination conditions). Optimising for the information gained at multiple frequencies reduces the performance at high frequencies but improves the information gained at low frequencies. Finally, an optimisation to minimise the average variance of a range of frequencies (orange) weighs the poor performing low order terms even more, improving them at the cost of the higher frequencies yet again. The average variance values in the legend reflect (unsurprisingly) that this indeed improves the performance in this metric. While not used in this work as our metric is the variance bound of an estimator (from the Fisher information), the sensitivity of the wavefront sensor is marked on the right y-axis to allow for comparison with other publications.

We note one difference with respect to the plots shown in Haffert et al. (2023): the behaviour of the Fisher information at small spatial frequencies approached zero but remains non-zero in this work. In Haffert et al. (2023), low frequency modes were not normalised and hence each Fourier mode approached the (undetectable) piston mode, while in this work the normalisation means that low frequency sine modes approach the tip/tilt Zernike.

3.2. Performance in different scenarios

3.2.1. Aperture

First, we qualitatively evaluate the performance of the system for different apertures. Figure 3 illustrates the optimised system for the Magellan, Giant Magellan Telescope (GMT) and ELT apertures. In the top row, we visualise the amplitude of the electric field after the first pair of PIAA lenses. As expected, the apodisation concentrates the starlight towards the centre of the aperture. For non-circularly symmetric apertures, however, the shape is clearly distorted. Next we show the reference intensity (response of the system to a flat wavefront) I_0 . All apertures share the behaviour where light from the geometric pupil is diffracted out into a circle that circumscribes it. There is also a weak halo. Next, we show the response of the wavefront sensor to a high frequency Fourier mode at the pupil, both without and with a pair of inverse PIAA lenses. Without the inverse optics, the pupil geometry remains distorted and contours of the intensity change are no longer vertical. Near the centre of the pupil these changes are more concentrated, requiring more pixels to sample the changes. This would reduce the sensitivity of the sensor in the faint limit, where read noise dominates per pixel. On the other hand, the system with an inverse PIAA (last row) has restored geometry and uniform sampling.

3.2.2. Stellar magnitude

Next, in Figure 4, we evaluate the PIAA-ZWFS with varying flux, and optimise the design for both bright and faint operation. We continue to use the loss metric (average variance of a maximum likelihood estimator) normalised per photon to observe the underlying trend. We simulate both a photon counting camera (read noise $0.5e^-$) and a low quality camera (read noise $10e^-$) running at 1kHz with an end-to-end system throughput of 30%.

The shape of the loss function with decreasing flux is flat in the bright regime, before sharply increasing at an elbow. Optimising the system anywhere in the flat region (such as the 0 or

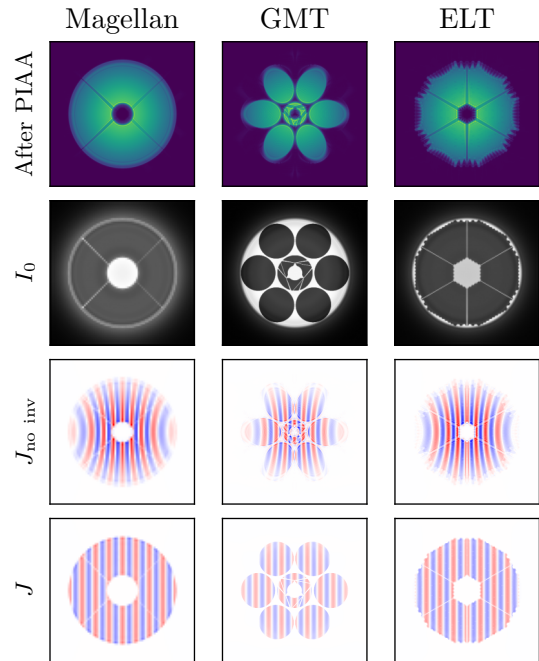


Fig. 3: PIAA ZWFS designs and behaviour for different apertures. The apodization profile after the first lens pair (1st row, showing $|E|$) concentrates the light in the centre of the pupil. The reference intensity (2nd row, now at the sampling of the detector) scatters some light outside the pupil. The intensity change for an applied Fourier mode (3rd and 4th rows) shows a strong response, however if the inverse PIAA is omitted (3rd row) the pattern is distorted and sensitivity is lost due to the higher sampling required.

10 magnitude optimisation for $\sigma_R = 0.5e^-$) leads to the same result. This means that a single PIAA-ZWFS should suffice for all bright stars. After the turnoff, however, it is possible to optimise the system for significantly better performance, gaining about 0.75 magnitudes. The reference intensities (bottom) behave as expected: in the faint case, starlight is concentrated, with less diffraction outside the geometric pupil.

Even though Equation 5 shows that changing overall flux is not the same as changing read noise, the behaviour for a higher read noise camera is qualitatively very similar, with the performance degradation occurring about $2.5 \log_{10}((10/0.5)^2) \approx 8.5$ magnitudes earlier.

We note that this analysis assumed a constant number of modes between bright and faint modes for a valid comparison. However, in order to fully optimise a system for faint operation the number of modes corrected and the number of pixels read should be carefully considered given the requirements of the adaptive optics system.

3.2.3. Bandwidth

An important factor of any wavefront sensor is how the performance changes with bandwidth, since a large bandwidth is ultimately what provides photons, enabling AO systems to run at fast speeds and on fainter targets. In this experiment we keep the number of photons per frame fixed (and in the photon-noise limited regime) and change the fractional bandwidth of the input field.

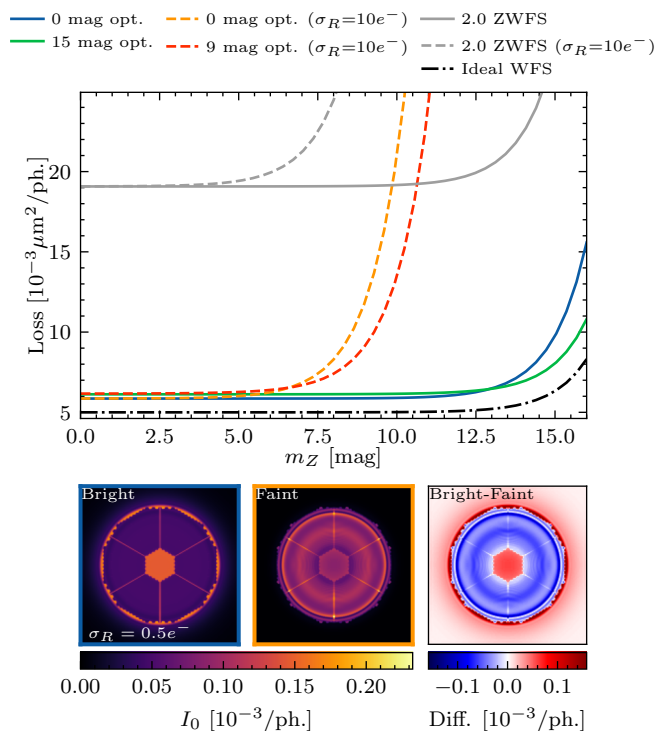


Fig. 4: PIAA-ZWFS performance on the ELT (240 pixels across the pupil diameter). *Top*: Loss (average variance of the maximum likelihood estimate) normalised to photon count as a function of stellar magnitude. Different lines correspond to designs optimised for different read noise and/or stellar magnitude. The ideal WFS has the same read noise as the other sensors with solid lines (0.5e⁻). *Bottom*: reference intensities for the bright (left) and faint (middle) design, along with the difference of the two (right). The faint design has put the flux into less pixels, particularly outside of the pupil, minimising the effect of read noise.

Figure 5 illustrates how the performance of the wavefront sensors studied degrades with wider bandwidth. We optimise four different designs: a combination of monochromatic vs. 0.2 fractional bandwidth, and no PIAA vs PIAA. All optimised designs outperform conventional Zernike wavefront sensors and approach the ideal wavefront sensor bound in the narrowband limit.

Inspecting the converged phase mask designs in the bottom of Figure 5, we find that the inclusion of a PIAA results in the removal of mask rings in the wings of the Airy pattern, explaining the reduction of chromatic behaviour. Furthermore, optimising the designs for broader bandwidths (orange) results in a phase mask that is more concentrated, where the Airy pattern is almost identical at different wavelengths.

Ultimately, our results demonstrate that, whilst not completely insensitive to chromatic effects, the PIAA ZWFS can be designed for robustness to different wavelengths. Future work can address more complex designs, such as doublet lenses or reflective optics, possibly with Wynne correctors (Wynne 1979).

3.2.4. Stellar size

With the coming generation of ELTs, some scientifically interesting targets can no longer be assumed to be point sources. We explore the effect of stellar size on different wavefront sensors,

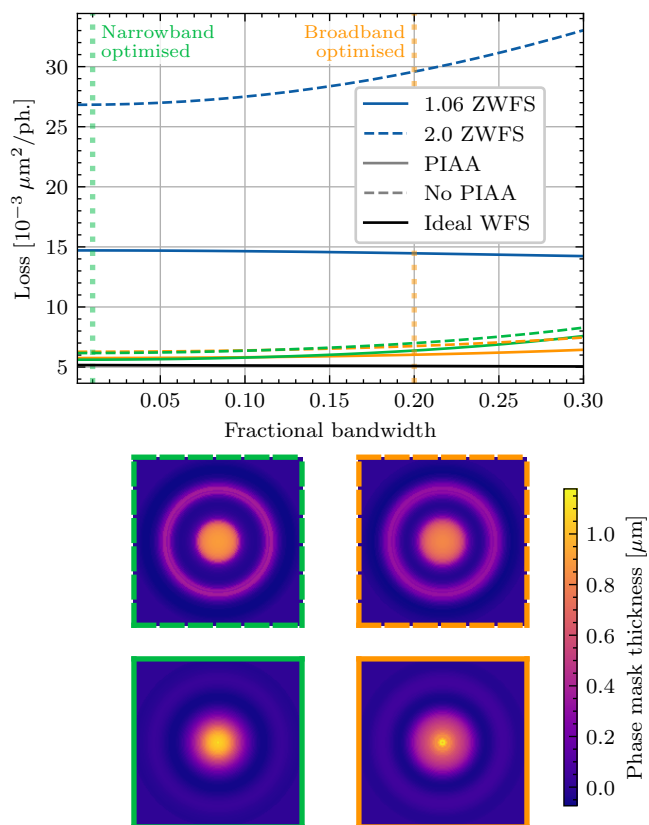


Fig. 5: Wavefront sensor performance for different bandwidth. *Top*: The average variance of the prediction as a function of changing bandwidth. A Zernike WFS with dot size $2\lambda/D$ (2 ZWFS, blue dashed) shows a large (23% at 0.3 bandwidth compared to monochromatic) degradation of performance with increasing bandwidth. We illustrate versions of our designs optimised for 20% (orange) and 1% (green) bandwidth. Designs optimised for larger bandwidths degrade less when compared to the 2 ZWFS. Designs without a PIAA (dashed) degrade faster and perform worse. The PIAA ZWFS designed for broadband operation only performs 12% worse when compared to the monochromatic case. An ideal, achromatic wavefront sensor (black) performs well at all bandwidths. *Bottom*: The phase masks from the optimised designs, with border colour matching the top plot. The addition of the PIAA results in a more concentrated phase mask, explaining the better robustness of chromatic effects. Optimising for a larger bandwidth increases the size of the dot slightly and makes it more uniform, except at the very centre.

and design PIAA ZWFS's that are optimised for resolved targets. We modify the simulator to inject a uniform disk as the source on sky by incoherently integrating over a range of tip/tilt values (approximated as a sum over 3 radial samples and 6 angular samples on a polar grid). This is done in the photon-limited regime as these targets are also bright, with the ELT aperture for a wavefront sensor operating in the Z band.

Figure 6 shows the results from this experiment. The top plot depicts the performance of the wavefront sensor on a logarithmic scale as a function of stellar diameter D_\star . Almost all wavefront sensors perform worse as the stellar size grows, with the exception of the 2 ZWFS (which begins with relatively poor performance). In particular, the “ideal” wavefront sensor – which is quantum optimal for point sources – rapidly becomes suboptimal. Our approach is able to outperform it for $D_\star > 0.8\lambda/D$. We

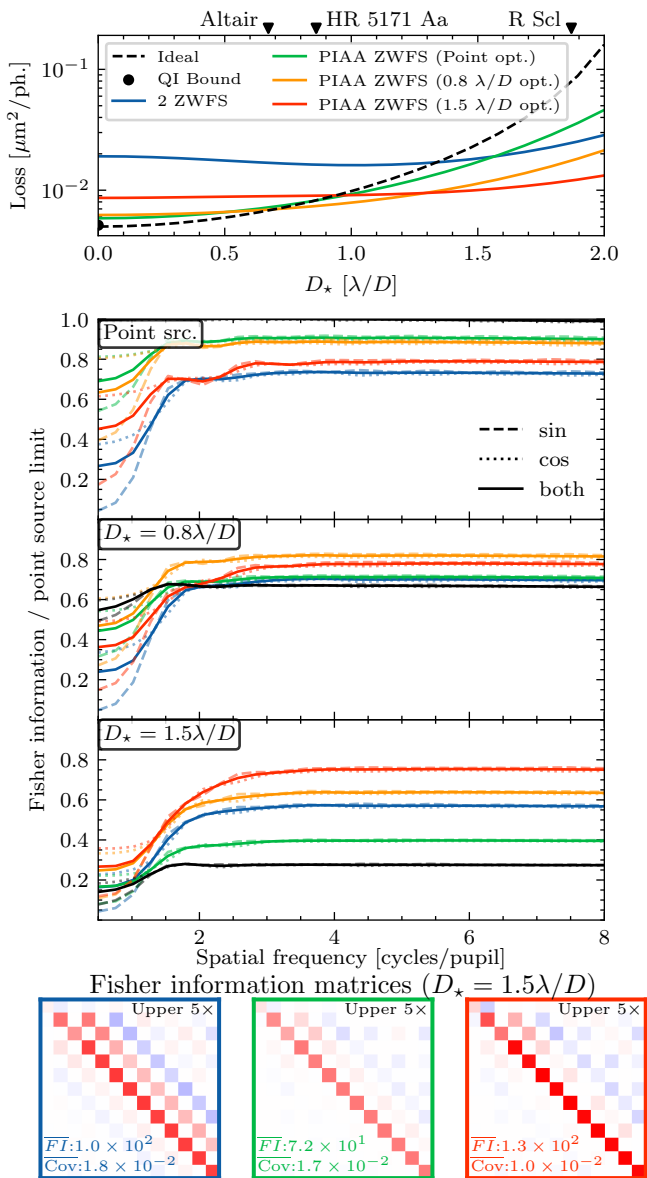


Fig. 6: Resolved objects on the ELT, Z band. *Top*: WFS performance as a function of stellar size. Performance declines with coherence, notably for the ideal WFS (black, dashed) which meets the quantum information (QI) bound (black dot) for point sources. Our optimised designs for resolved objects (orange and red) outperform the “ideal” system for $D_\star = 0.8\lambda/D$. *Middle*: Information (relative to the point source limit) vs. spatial frequency for each WFS at a different stellar size; solid lines illustrate the quadrature average of sine/cosine terms. Only the resolve-optimised PIAA-ZWFS resists sensitivity loss as stellar size increases. *Bottom*: Fisher information matrices for the 2 ZWFS (blue), point-optimised PIAA ZWFS (green) and the resolve-optimised (1.5 λ/D) PIAA ZWFS (red), with a common colorbar. Insets state the average Fisher information (FI) and trace of the covariance matrix (Cov) per photon. While the 2 ZWFS has larger values on the diagonal than the point-optimised PIAA-ZWFS, the cross correlation terms (non-zero off diagonal) result in the same variance value. The resolve-optimised design has both high information and low cross terms.

hypothesise that this rapid degradation is because the ideal wavefront sensor is sensitive to tip/tilt modes, and exploits coherence

which these larger sources do not have. The middle plots show the sensitivity behaviour as a function of spatial frequency. The sensitivity of the ideal wavefront sensor reduces approximately equally at all frequencies, while designs that are optimised for resolved sources (orange and red) maintain consistent behaviour for source sizes smaller than the design value. All wavefront sensors struggle to constrain tip/tilt like modes (dotted lines at low frequencies) when the source becomes resolved.

The middle plots (up to a square root) are commonly used in the literature to support one wavefront sensor over another. In the bottom plot, we show an example where this visualisation has the potential to obscure wavefront sensing performance where multiple aberrations are present. Looking at the $D_\star = 1.5\lambda/D$ case alone, one might come to the conclusion that the 2 ZWFS (blue) is equal to or more sensitive than the point-optimised PIAA ZWFS (green) at all frequencies. If we inspect the Fisher information matrices, we do indeed observe that the 2 ZWFS diagonal has (almost 40%) larger values than the PIAA ZWFS, however this also contains significant cross correlation off the diagonal. This means that the responses of the wavefront sensor to orthonormal modes aren’t orthogonal, and that errors have the capacity to couple between different aberration coefficients. This is reflected in the average of the diagonal elements of the (not pictured) covariance matrix (Cov), for which the PIAA ZWFS is marginally better. The resolve-optimised PIAA ZWFS (red) maintains high information content along the diagonal whilst also minimising off-diagonal components. While the discrepancy between the sensitivity plots and full Fisher matrix is most clearly seen for the resolved source case, we note that this behaviour can occur in any system.

3.3. Ablation study

We now turn to a direct comparison between different sensors in a typical case: a Z band wavefront sensor on the Magellan telescope with 60 actuators across the pupil in the photon limited regime. To highlight the importance of each component shown in Figure 1, we run optimisations with all possible combinations of system architecture in addition to the standard 1.06 ZWFS and proposed 2 ZWFS.

Table 1: Ablation study for our optimised system. Loss (normalised average variance of a maximum likelihood estimator) and sub-optimality as a fraction of an ideal wavefront sensor. The use of PIAA lenses and an annular mask (AM) instead of a simple dot each provide improvements.

System	PIAA	AM	Loss (10^{-3} ↓)	Sub-opt. (%)
Ideal			5.12	
1.06 ZWFS			14.5	183
2.0 ZWFS			29.5	475
Ours			7.35	44
Ours	✓		6.29	23
Ours		✓	6.72	31
Ours	✓	✓	6.01	17

Table 1 contains the results of the ablation study for our system. Results are presented as absolute loss (the average variance per mode per photon of a maximum likelihood estimator) and the sub-optimality of the sensor as a percentage of the loss of an ideal wavefront sensor. We note that reflections aren’t accounted for as this can depend on manufacturing decisions, but due to

the normalisation of the loss by the flux the effect can be easily accounted for. For example, assuming a Thorlabs ‘B’ coating with an average reflectance of 0.26% per surface, the resulting loss for the PIAA and annular mask system (14 surfaces) is 6.23 while the annular mask only (6 surfaces) system has a loss of 6.83. Hence the use of the PIAA lenses remains a net positive.

From these results we identify that the PIAA ZWFS closes the gap between the ideal wavefront sensor and the 1.06 ZWFS by around an order of magnitude (17% sub-optimality rather than 183%), and a factor 2.5 compared to an optimised ZWFS. We do, however, note that the exact value depends on the basis selected.

3.4. Wavefront reconstruction

We now validate our optimisation approach and explore the dynamic range of the PIAA-ZWFS by reconstructing aberrated wavefronts. We generate different turbulence OPD screens with a power law, project them onto a basis and then try to reconstruct the basis terms. Errors are only measured relative to the aberrations that are spanned by the basis set. To show the flexibility of the above optimisation, we use the same optical models as from the ablation study, changing only the OPD basis to now consider the first 45 Zernikes (excluding piston) rather than a one dimensional Fourier basis. We show the reconstructor performance in a photon limited regime and add Poisson noise to the data.

Linear reconstructors are created by using the same auto-differentiation framework to calculate the interaction matrix. The non-linear reconstructors are differentiable forwards models. Initialised from a flat phase at the pupil, these models fit modal coefficients using BFGS, minimising the logarithm of the probability mass function for the Poisson distribution. While this is impractical for real time control, it shows the realistic dynamic range, identifying the aberration region where real-time non-linear reconstructors (such as neural networks) should focus.

Figure 7 shows the reconstructor error over the aperture for different sensors using a linear (top) and non-linear (bottom) reconstruction method. The results are binned and the median is presented as the line with the 16-84 percentile shaded. In the low aberration case, the PIAA-ZWFS is comparable with an ideal wavefront sensor while the classical 1.06 ZWFS performs worse. This is as expected from the optimisation results. As the aberrations grow larger, the non-linear behaviour appears in all sensors before the 10 nm RMS point, growing until there is no correct estimate after 100 nm RMS. Using a non-linear reconstructor, however, we can extend the range of photon noise limited estimates by an order of magnitude, before catastrophic failures of the reconstruction emerge around 100 nm RMS. This point appears marginally earlier for the ideal wavefront sensor and the PIAA ZWFS compared to the classical ZWFS. These large aberrations result in phase wrapping, where the aberration producing the sensor image is not the same local minimum in common with the initialisation point. In the large aberration regime with many modes choosing the right initialisation point becomes intractably hard. As this simulation is conducted with a central wavelength of 900 nm, we expect peak-to-valley changes of order 2π radians at around 100 nm RMS. In our experience, varying the basis set tweaks the exact failure point (whilst maintaining the same overall shape in both linear and non-linear reconstruction), indicating that dynamic range weakly depends on the aberration distribution.

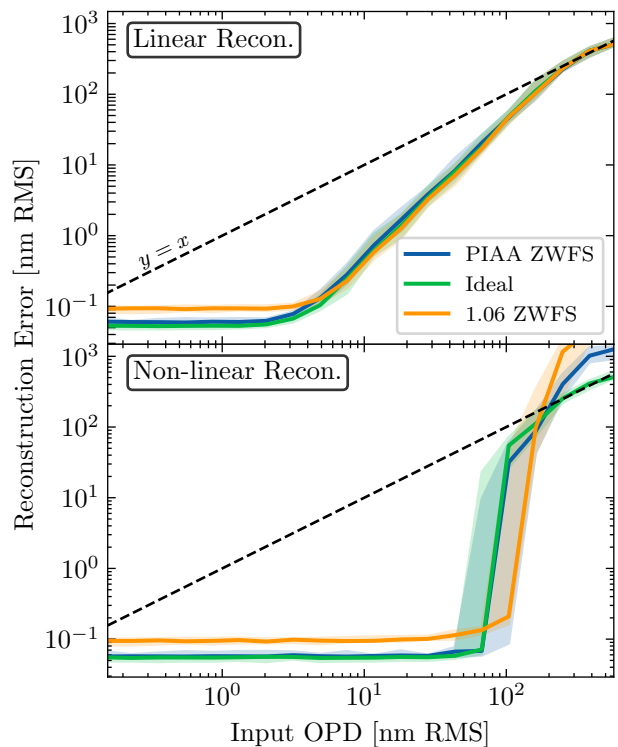


Fig. 7: Wavefront estimate errors under varying input aberration size for different wavefront sensors and reconstructors for a Zernike aberration basis. Results are binned by input OPD, with the line showing the median and the shaded area showing the 16-84 percentiles of each bin. The black dashed line indicates no reconstruction ($y = x$). The PIAA ZWFS outperforms the classical ZWFS ($1.06\lambda/D$ dot diameter) and is comparable with the ideal point source wavefront sensor. The performance of all linear reconstructors degrades equally fast with non-linear behaviours. A non-linear reconstructor performs well for all sensors and extends the range by over an order of magnitude.

4. Discussions

It is evident that the PIAA-ZWFS effectively closes the gap towards the fundamental sensing limit in the high Strehl regime. The degrees of freedom given in the design space (namely PIAA sag and annular rings of the phase mask) enable a family of designs that can be optimised for different apertures, flux levels, aberration modes, bandwidths and source distributions. The increased sensitivity to phase aberrations compared to the classical ZWFS is due to mode matching, where the reference beam is shaped to match that of a beam from a pinhole the size of the phase mask. The use of PIAA lenses also increases the bandwidth of the designs and makes the phase mask less extended and hence easier to fabricate.

In early experiments we were able to replicate a saturation of the sensitivity bound for high spatial frequencies when optimising for the average Fisher information and when sampling the detector with enough pixels, first observed in Haffert et al. (2023). However, in all adaptive optics systems, phase aberrations do not occur at only a single frequency. It is not the sensitivity/information gain of any particular mode that matters, but rather the uncertainty on the reconstruction solution of a maximum likelihood estimator that determines the performance (in, e.g. Strehl). Hence, our optimisation metric of the trace of the covariance matrix correctly manages correlations between re-

sponses to different orthogonal phase aberrations, and weighs the sensitivity appropriately when optimising for a generic quantity such as Strehl. This behaviour is most clearly seen in the last row of Figure 6, where our resolve-optimised design has both large information content and low average variance (via low cross-talk), particularly compared to the ZWFS. The validity of our metric is also reinforced by the reconstruction results shown in Figure 7, where the optimised design approaches an ideal wavefront sensor and outperforms the ZWFS in the photon and low aberration limit.

For true end-to-end optimisation, the covariance matrix is fed into an application specific loss function—we do not do this, instead showing the system as a whole for a generic task. Priors can be easily incorporated by adding a matrix to the Fisher information matrix before inversion. Another generic metric could be the log determinant (corresponding to minimising the volume of the confidence ellipsoid); we found very similar results for either metric on preliminary experiments and decided the average variance was easier to interpret.

Whilst significantly closer to the information limit than other designs explored here, the PIAA-ZWFS is still sub-optimal, most noticeably for low order modes (Figure 6, point source case), although it still outperforms existing methods. This sub-optimality is related to the light scattered outside the pupil observed in Figure 3. As the beam is tilted off the phase mask, the amount of light scattered is reduced. This decrease, however, doesn't contribute to the information gained as the sign of the change is ambiguous. For higher spatial frequencies, this is effectively a change in the intensity of the reference beam, which only changes quadratically with the applied aberration. In existing systems, however, the light outside the pupil is still practically useful, providing telemetry information and a estimate of the on-axis Strehl ratio. A truly ideal wavefront sensor would not have access to this additional debugging information.

A recent preprint by Trzaska & Ashok (2025) presented the piston-adapted wavefront sensor (PAWS), a sensor design that can, in principle, phase shift the piston mode alone by $\pi/2$ (and hence is quantum optimal in the high Strehl regime). The system presented requires at least 42 glass surfaces and 4 mirrors, compared to just 14 glass surfaces for the PIAA-ZWFS presented here. Assuming the same coating as before for the glass surfaces and a standard 2% loss for the mirrors, the PAWS loss (in the context of Table 1 as the ideal wavefront sensor) becomes 6.19, compared to the reflection loss adjusted value of 6.23 calculated before for the PIAA-ZWFS. These are comparable at the level of implementation details and the choice of basis as discussed previously. Furthermore, we believe the PIAA-ZWFS is significantly easier to manufacture and align than the PAWS, however implementation in hardware is left as future work.

Finally, we consider the importance of the dynamic range of the wavefront sensor presented. Despite the gain in sensitivity provided by the PIAA-ZWFS, dynamic range is not lost in linear reconstructors relative to the classical ZWFS, nor non-linear reconstructors relative to an ideal wavefront sensor. Hence, we believe that the same reconstruction techniques that are being developed for the ZWFS apply to the PIAA-ZWFS. As a second stage wavefront sensor, the sensing requirements on reconstruction depend on the first stage residuals and the parameters of the second stage control loop. If operating in the non-linear region, different strategies are possible. We note that a closed loop system could converge even with the linear reconstructor, given the timescale of the evolution is slower than the convergence time. Another option is to leverage fast non-linear reconstructors, such as neural networks which have been demon-

strated on-sky for pyramid wavefront sensors (Landman et al. 2025). Finally, there is also the possibility to alter the hardware, capturing sensor frames in multiple wavelengths and/or polarisations simultaneously. Multiple wavelengths have been shown to improve dynamic range significantly in simulation (Darcis et al. 2025) and also has good synergies with emerging technologies such as microwave kinetic inductance detectors (MKIDs) (Mazin et al. 2019). Similarly, a vector ZWFS has been shown in a lab setting to admit a much larger dynamic range (Doelman et al. 2018; Wenger & Wallace 2025). The optimisation framework presented in this work can be easily adapted to these cases for future work.

5. Conclusions

Second stage wavefront sensors are a critical part of extreme AO systems in high contrast and high angular resolution imaging. Sensors that provide the most information about phase aberrations per photon enable the best systems to provide better correction by running at faster speeds or on fainter targets. Similarly, these sensors would significantly reduce the time needed to reach picometre knowledge for high contrast instruments in space. While the information limits of wavefront sensing have been known for some time, the search for architectures that reach these limits is ongoing. The PIAA-ZWFS presented in this work makes significant strides towards this target.

While it is possible to optimise the PIAA-ZWFS architecture to saturate the limit at high spatial frequencies, we instead stress the importance of using the variance of an unbiased, maximum likelihood estimator as the metric for performance. This choice more accurately reflects the closed loop residuals and correctly accounts for correlations between phase aberrations. Through this framework we optimise the PIAA-ZWFS in a differentiable simulator. Our results demonstrates the sensor functions well on a range of apertures, bandwidths, fluxes and stellar sizes. Our sensor outperforms the “ideal” wavefront sensor on extended objects with diameter $> 0.8\lambda/D$. Our ablation study demonstrates that each complexity added to the system improves performance significantly. For the basis selected, we close the gap to the ideal wavefront sensor by an order of magnitude compared to the previous state-of-the-art sensor – the ZWFS. Finally, we verify that the sensor's dynamic range is not drastically reduced by the gain in sensitivity through reconstruction of a mixture of phase aberrations.

There are several exciting avenues of future work. Most critically, hardware development and verification of the simulation results presented this work are needed. Different processes can be employed to manufacture the phase masks presented in this work, such as grayscale lithography. A less explored process would involve a metasurface phase mask, which could, in principle, enable wavefront sensing and coronagraphy with a single optic. As part of the hardware development an understanding of the practicalities of the system are important, namely how the system degrades with misalignment and manufacturing imperfections. Another practical avenue of future work is to explore how, given a list of desired targets, different operating modes of a manufactured PIAA-ZWFS could be designed while holding the PIAA lenses common among all modes. Finally, the dynamic range of the sensor should be tested empirically, with both software (such as non-linear, neural network reconstructors) and hardware (such as multiple wavelength images) modifications.

Acknowledgements. The authors acknowledge funding from NWO VI.Vidi.233.144. This work was performed using the compute resources from the Academic Leiden Interdisciplinary Cluster Environment (ALICE)

provided by Leiden University. We would like to thank R. Landman, M. Ireland, M. Mars and J. K. Wallace for helpful discussions. Microsoft Copilot was used in developing the software for this work.

References

- Bracewell, R. & Kahn, P. B. 1966, *American Journal of Physics*, 34, 712
- Chambouleyron, V., Fauvarque, O., Plantet, C., et al. 2022, in *Adaptive Optics Systems VIII*, Vol. 12185, SPIE, 932–944
- Chambouleyron, V., Fauvarque, O., Plantet, C., et al. 2023, *Astronomy & Astrophysics*, 670, A153
- Chambouleyron, V., Wallace, J. K., Jensen-Clem, R., & Macintosh, B. 2024, *Optics Express*, 32, 47706
- Chang, S., Guo, X., & Ni, X. 2018, *Annual Review of Materials Research*, 48, 279
- Darcis, M., Haffert, S., Chambouleyron, V., et al. 2025, *Astronomy & Astrophysics*, 701, A157
- Doelman, D. S., Fagginger Auer, F., Escuti, M. J., & Snik, F. 2018, *Optics letters*, 44, 17
- Doelman, D. S., Snik, F., Warriner, N. Z., & Escuti, M. J. 2017, in *Techniques and Instrumentation for Detection of Exoplanets VIII*, Vol. 10400, SPIE, 224–235
- Fauvarque, O., Janin-Potiron, P., Correia, C., et al. 2019, *Journal of the Optical Society of America A*, 36, 1241
- Fletcher, R. 2013, *Practical methods of optimization* (John Wiley & Sons)
- Forbes, G. W. 2007, *Optics express*, 15, 5218
- Grushina, A. 2019, *Advanced Optical Technologies*, 8, 163
- Guyon, O. 2003, *Astronomy & Astrophysics*, 404, 379
- Guyon, O. 2005, *The Astrophysical Journal*, 629, 592
- Guyon, O. 2018, *Annual Review of Astronomy and Astrophysics*, 56, 315
- Haffert, S. Y., Males, J. R., & Guyon, O. 2023, arXiv preprint arXiv:2310.10889
- Hoffnagle, J. A. & Jefferson, C. M. 2000, *Applied optics*, 39, 5488
- Kasper, M., Urta, N. C., Pathak, P., et al. 2021, arXiv preprint arXiv:2103.11196
- Landman, R., Haffert, S. Y., Long, J., et al. 2025, *Astronomy & Astrophysics*, 696, L1
- Landman, R., Keller, C., Por, E. H., et al. 2022, in *Adaptive Optics Systems VIII*, Vol. 12185, SPIE, 2582–2593
- Males, J. R., Close, L. M., Haffert, S. Y., et al. 2024, in *Ground-based and Airborne Instrumentation for Astronomy X*, ed. J. R. Vernet, J. J. Bryant, & K. Motohara (Yokohama, Japan: SPIE), 34
- Males, J. R., Fitzgerald, M. P., Belikov, R., & Guyon, O. 2021, *Publications of the Astronomical Society of the Pacific*, 133, 104504
- Mazin, B. A., Bailey, J., Bartlett, J., et al. 2019, arXiv preprint arXiv:1908.02775
- N'Diaye, M., Dohlen, K., Fusco, T., & Paul, B. 2013, *Astronomy & Astrophysics*, 555, A94
- Paterson, C. 2008, 139, 012021
- Rader, J., Lyons, T., & Kidger, P. 2024, arXiv preprint arXiv:2402.09983
- Ragazzoni, R. & Farinato, J. 1999, *Astronomy and Astrophysics*, v. 350, p. L23-L26 (1999), 350, L23
- Slepian, D. 1965, *Journal of the Optical Society of America*, 55, 1110
- Soummer, R., Pueyo, L., Sivaramakrishnan, A., & Vanderbei, R. J. 2007, *Optics Express*, 15, 15935
- Steeves, J., Wallace, J. K., Kettenbeil, C., & Jewell, J. 2020, *Optica*, 7, 1267
- Trzaska, J. & Ashok, A. 2025, arXiv preprint arXiv:2511.05707
- Wenger, T. & Wallace, J. K. 2025, *Optics Letters*, 50, 726
- Wyne, C. 1979, *Optics Communications*, 28, 21
- Zernike, F. 1934, *Monthly Notices of the Royal Astronomical Society*, Vol. 94, p. 377-384, 94, 377

Appendix A: Derivation of Fisher information bounds

A general result for the derivative of the intensity with respect to a parameter is

$$\frac{\partial_\beta I}{N_{\text{ph}}} = \partial_\beta (|E_o|^2) \quad (\text{A.1})$$

$$= \partial_\beta (E_o^* E_o) \quad (\text{A.2})$$

$$= \partial_\beta (E_o^*) E_o + E_o^* \partial_\beta (E_o) \quad (\text{A.3})$$

$$= \partial_\beta (E_o)^* E_o + E_o^* \partial_\beta (E_o) \quad (\text{A.4})$$

$$= 2\Re \{E_o^* \partial_\beta E_o\}, \quad (\text{A.5})$$

where we have used the fact that the derivative and complex conjugate are interchangeable.

A.1. Sensitivity to photon noise

This bound was previously demonstrated in Paterson (2008). Here we present an alternative proof in a Fisher information framework.

This is a proof from first principles, starting from considering a single pixel with index j . We start by considering the measured intensity \hat{I}_j (which is a random variable), such that the probability distribution of the pixel is given by a Poisson distribution

$$f_j(x_j|\theta) = \Pr(\hat{I}_j = x_j) = \frac{I_j^{x_j} \exp(-I_j)}{x_j!}. \quad (\text{A.6})$$

The Fisher information with respect to a parameter θ then is

$$\text{FI}_j[\theta] = \sum_{x_j=0}^{\infty} \frac{(\partial_\theta f_j(x_j|\theta))^2}{f_j(x_j|\theta)} \quad (\text{A.7})$$

Applying the derivative and simplifying produces

$$\text{FI}_j[\theta] = (\partial_\theta I_j)^2 \frac{1}{I_j^2} \sum_{x_j=0}^{\infty} \frac{I_j^{x_j} \exp(-I_j) (x_j - I_j)^2}{x_j!} \quad (\text{A.8})$$

$$= \frac{(\partial_\theta I_j)^2}{I_j^2} \text{Var}[\hat{I}_j] \quad (\text{A.9})$$

$$= \frac{(\partial_\theta I_j)^2}{I_j}. \quad (\text{A.10})$$

This agrees with the expression previously Haffert et al. (2023). Note that for cross terms one can change the numerator to $(\partial_{\theta_1} I_j)(\partial_{\theta_2} I_j)$.

Proof of the bound Each pixel can be treated as an independent (for Poisson noise) experiment, and hence the Fisher information for the whole frame is given by

$$\text{FI}_{\text{Pois}}[\theta] = \sum_j \frac{(\partial_\theta I_j)^2}{I_j} \quad (\text{A.11})$$

$$= \left\| \frac{\partial_\theta I}{\sqrt{I}} \right\|^2 \quad (\text{A.12})$$

$$= N_{\text{ph}} \left\| \frac{2\Re \{E_o^* \partial_\theta E_o\}}{|E_o|} \right\|^2. \quad (\text{A.13})$$

Observe that $\Re \{E_o^* \partial_\theta E_o\} = |E_o| |\partial_\theta E_o| \cos(\dots) \leq |E_o| |\partial_\theta E_o|$, and hence

$$\frac{\text{FI}_{\text{Pois}}[\theta]}{N_{\text{ph}}} \leq 4 \left\| |\partial_\theta E_o|^2 \right\| = 4, \quad (\text{A.14})$$

with the last step follows the same argument as Paterson (2008): $\partial_{a_k} E_o = iC\{W_k E_i\}$, which is a unitary transformation of an orthonormal set.

A.2. Sensitivity to read noise

Next we consider a read noise only case in order to compare with the proof in Chambouleyron et al. (2023), but note that the proof is identical for a pixel with both Poisson and read noise by simply changing the variance from σ_R^2 to $I_j + \sigma_R^2$. The distribution sampled is for a single pixel (indexed by j), and is a normal distribution i.e. $X \sim \mathcal{N}(I_j, \sigma_R^2)$, where σ_R is the read noise. The Fisher Information with respect to a parameter is then

$$\text{FI}_\theta = \mathbb{E}_x \left[\left(\frac{\partial}{\partial \theta} \log f(x; \theta) \right)^2 \right], \quad (\text{A.15})$$

where x is the integration variable from the normal distribution

$$f(x; \theta) = \frac{1}{\sqrt{2\pi\sigma_R^2}} \exp\left(-\frac{(x - I_j(\theta))^2}{2\sigma_R^2}\right). \quad (\text{A.16})$$

Applying the chain rule and factoring out terms that do not depend on x we obtain

$$\text{FI}_\theta = \left(\frac{1}{2\sigma_R^2} \frac{\partial I_j(\theta)}{\partial \theta} \right)^2 \mathbb{E}_x \left[\left(\frac{\partial}{\partial (I_j(\theta))} (-(x - I_j(\theta))^2) \right)^2 \right] \quad (\text{A.17})$$

$$= \left(\frac{1}{\sigma_R^2} \frac{\partial I_j(\theta)}{\partial \theta} \right)^2 \mathbb{E}_x \left[(x - I_j(\theta))^2 \right] \quad (\text{A.18})$$

$$= \frac{1}{\sigma_R^2} \left(\frac{\partial I_j(\theta)}{\partial \theta} \right)^2 \quad (\text{A.19})$$

$$= \frac{(\partial_\theta I_j(\theta))^2}{\sigma_R^2}. \quad (\text{A.20})$$

This is for an individual pixel j . Again one can sum this over all pixels

$$\text{FI}_\theta = \sum_j \frac{(\partial_\theta I_j(\theta))^2}{\sigma_R^2}. \quad (\text{A.21})$$

The result agrees with Eq. (24) of Chambouleyron et al. (2023) after noting that our intensity I is not normalised to have a sum of unity over the image (and instead sums to N_{ph}).

Proof of the bound Similar to before, the bound is now given by

$$\text{FI}_\theta = \frac{1}{\sigma_R^2} \|\partial_\theta I\|^2 \quad (\text{A.22})$$

$$= \frac{N_{\text{ph}}^2}{\sigma_R^2} \left\| 2\Re \{E_o^* \partial_\theta E_o\} \right\|^2 \quad (\text{A.23})$$

$$= \frac{4N_{\text{ph}}^2}{\sigma_R^2} \left\| \Re \{E_o^* \partial_\theta E_o\} \right\|^2 \quad (\text{A.24})$$

$$\leq \frac{4N_{\text{ph}}^2}{\sigma_R^2} \left\| |E_o| |\partial_\theta E_o| \right\|^2. \quad (\text{A.25})$$

This is still bounded to a value of $4N_{\text{ph}}^2/\sigma_R^2$. To see this, consider the expansion of the norm $\sum_j |E_{o,j}|^2 |\partial_\theta E_{o,j}|^2$, which, by the Cauchy-Schwarz inequality, is bounded by

$$\sqrt{\sum_j |E_{o,j}|^2 \sum_j |\partial_\theta E_{o,j}|^2} \leq 1, \quad (\text{A.26})$$

where the first sum is less than or equal to unity by energy conservation (equality for a lossless system) and the second follows the same argument as in the previous subsection. Hence, the bound for the Fisher information for phase estimation in the read noise only case is 4 units read noise variance per radian per photon.

A.3. Wavefront sensors under both amplitude and phase errors

A.3.1. Classical bound

Instead suppose the electric field at the input is given by

$$E_i = A \exp \left(i \sum_k (a_k W_k) - \sum_k (b_k W_k) \right), \quad (\text{A.27})$$

where the second summation represents (log-)amplitude aberrations that exist on the same basis as the phase aberrations.

Applying Equation A.5 with the general Fisher information formula derived earlier (under Poisson noise only), we consider the quantity of the sum of the Fisher information of phase and amplitude

$$\text{FI}_{a_k} + \text{FI}_{b_k} = \sum_j \frac{(\partial_{a_k} I_j)^2 + (\partial_{b_k} I_j)^2}{I_j} \quad (\text{A.28})$$

$$= 4N_{\text{ph}}^2 \sum_j \frac{\Re\{E_o^* C \{iW_k E_i\}\}^2 + \Re\{E_o^* C \{-W_k E_i\}\}^2}{I_j} \quad (\text{A.29})$$

$$= 4N_{\text{ph}}^2 \sum_j \frac{\Im\{E_o^* C \{W_k E_i\}\}^2 + \Re\{E_o^* C \{-W_k E_i\}\}^2}{I_j} \quad (\text{A.30})$$

$$= 4N_{\text{ph}} \sum_j \frac{|E_o^* C \{W_k E_i\}|^2}{|E_o|^2} \quad (\text{A.31})$$

$$= 4N_{\text{ph}}^2 \sum_j |C \{W_k E_i\}|^2 \quad (\text{A.32})$$

Since W_k is orthonormal on the aperture, and C is unitary, the value of this integral is indeed $4N_{\text{ph}}$, for all indices k . This indicates the total information over amplitude and phase is constant for an arbitrary, lossless wavefront sensor. This implies there is *always* a trade-off between amplitude and phase sensitivity.

70 A.3.2. Quantum bound

In the quantum case the field is

$$\psi(x, y) = A(x, y) \exp \left(i \sum_k (a_k W_k) - \sum_k (b_k W_k) \right). \quad (\text{A.33})$$

The inner product in this space is defined as before. As in Trzaska & Ashok (2025), the quantum Fisher information matrix has elements mn given by

$$\text{FI}_{mn}^Q = 4\Re\{\langle \partial_m \psi, \partial_n \psi \rangle - \langle \partial_m \psi, \psi \rangle \langle \psi, \partial_n \psi \rangle\}, \quad (\text{A.34})$$

where m and n represent a phase or amplitude coefficient index and the inner product is as before but the first term now includes a complex conjugate (previously all terms were real). First we compute the phase-phase term for the same index

$$\text{FI}_{a_k a_k}^Q = 4\Re \left\{ \iint |C \{W_k E_i\}|^2 du dv - \langle C \{iW_k E_i\}, C \{E_i\} \rangle \langle C \{E_i\}, C \{iW_k E_i\} \rangle \right\}. \quad (\text{A.35})$$

Similarly for the amplitude-amplitude term

$$\text{FI}_{b_k b_k}^Q = 4\Re \left\{ \iint |C \{W_k E_i\}|^2 du dv - \langle C \{-W_k E_i\}, C \{E_i\} \rangle \langle C \{E_i\}, C \{-W_k E_i\} \rangle \right\}. \quad (\text{A.36})$$

Notice that the second term in each integral is identical but with an opposite sign. 80

Following Trzaska & Ashok (2025), the information of each component is not simply summed, but rather weighted by a matrix

$$C = \begin{bmatrix} I_K \cos^2(\theta) & 0 \\ 0 & I_K \sin^2(\theta) \end{bmatrix} \quad (\text{A.37})$$

with I_K as the the identity matrix of size K (the number of modes), and θ as a free parameter that determines how much weight is assigned to either phase or amplitude aberrations. As in the classic case, we assume equal weight to each ($\theta = \pi/4$). The weighted term then is

$$\frac{\text{FI}_{a_k a_k}^Q + \text{FI}_{b_k b_k}^Q}{2} = 4, \quad (\text{A.38})$$

where again we have used the orthonormality of W_k and the unitary transformation properties of C . This completes the proof that the trade-off between amplitude and phase information gain persists even when viewed through the lens of quantum information. 90

Appendix B: Additional results

B.1. Stellar magnitude (normalised)

To explore the rate of degradation at low photon count, we replot Figure 4 in Figure B.1, using the loss value normalised to each sensors own performance at $m_Z = 0$.

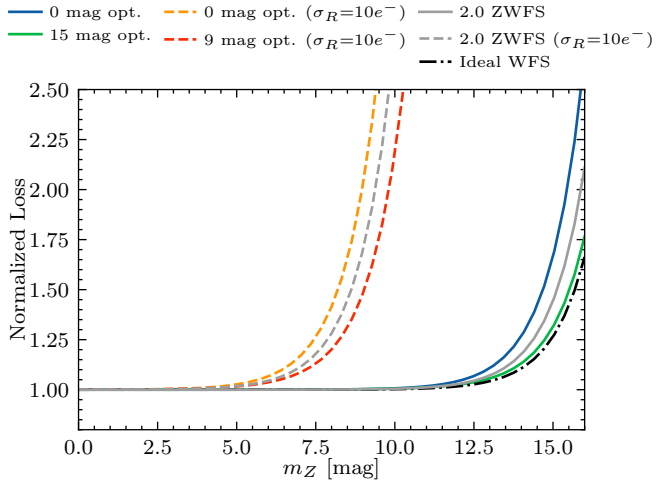


Fig. B.1: Same data as top of Figure 4, but normalised to the bright limit for each sensor. The faint PIAA-ZWFS degrades slower than a ZWFS in both the low and high read noise cases, and closely follows the ideal WFS at the same read noise.